Optimum Design and Technology Evaluation of Slip Permanent Magnet Generators for Wind Energy Applications.

Johannes H. J. Potgieter, *Student Member, IEEE* and Maarten J. Kamper, *Senior Member, IEEE*
Department of Electrical and Electronic Engineering
Stellenbosch University
Stellenbosch, South Africa
Email: kamper@sun.ac.za

***Abstract*—Recently a new type of wind generator concept known as a slip-synchronous permanent magnet generator was proposed. This is a gearless direct-drive generator which also connects directly to the grid, thus omitting the need for a power electronic converter. This generator consists of two machine units, a directly grid connected generator operating at synchronous speed and a directly turbine connected short-circuited generator unit. With the theory of designing the grid-connected permanent magnet generator unit well known, the focus in this study is on the identification and finite element design of the optimum turbine connected generator unit. Several different slip permanent magnet generator technologies are evaluated and a number of interesting novel concepts are introduced. These different generator units are optimised by means of finite element analysis for minimum mass, and very good results are obtained. The finite element results are verified by means of practical measurements.**

I. Introduction

The slip-synchronous permanent magnet generator (SS-PMG) concept is based upon a permanent magnet induction generator (PMIG), proposed in literature for the first time in 1926 by [1]. Several other studies have been launched since, as reported in [2]–[8]. The PMIG makes use of a second freely rotating permanent magnet (PM) rotor integrated within an induction machine as shown in Fig. 1(a). The PM-rotor supplies the magnetic flux within the machine and induces a voltage in the stator winding as shown in the equivalent circuit of Fig. 1(b). This, in principle, reduces the magnetizing current and improves the power factor of the machine.

The SS-PMG wind generator concept is introduced in [9] for the first time. This generator as shown in Fig. 2(a) and (b) consists of two PM machine units. It differs from the conventional PMIG system due to the fact that the two machine units are magnetically separated. The only linkage between the two units is the mechanical link through the common PM-rotor. The one generator unit is a normal permanent magnet synchronous generator (PMSG) with its stationary stator connected to the grid. The other generator unit, known as a slip permanent magnet generator (slip-PMG), operates on a principle similar to that of an induction generator with its short-circuited rotor connected to the turbine. This short-circuited rotor runs at slip speed with respect to the synchronously rotating PM-rotor.

The optimum design of the PMSG is well known as discussed in for example [10]. Apart from the SS-PMG system there are also other proposals which have been made in literature where PM wind generators are directly connected to the grid as for example in [11]–[13]. However, not so well known is how to set up the design criteria and obtain the optimum design of the slip-PMG unit. The novel SS-PMG concept proposed in [9] alleviates many of the constructional issues previously associated with PMIG type of systems. However, with the SS-PMG consisting of two direct-drive PM generators, a big question is the extra mass added to the design. Also, due to the volatility of PM material prices, the increase in PM mass can be considered as a potential drawback. The main aim in this paper is to reduce the mass of the slip-PMG unit without making the SS-PMG significantly more complex. With a clear design criteria lacking for the slip-PMG, this aspect is addressed in this paper by determining the most important performance constraints and to achieve the optimum design by evaluating several different slip-PMG concepts on the basis of active mass, PM content and manufacturability.

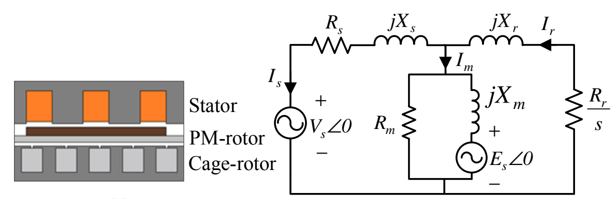

(a) (b)

Fig. 1: (a) Conventional PMIG configuration with the PM-rotor between the cage-rotor and stator and (b) the PMIG equivalent circuit.

II. Different slip-PMG Technologies

In this paper five different slip-PMG machine configurations are investigated where as in [9] only non overlap single layer (SL) and double layer (DL) winding slip-PMGs are investigated to some extent. Example structures of these two slip-PMGs are shown in Fig. 3(a) and (b) respectively. The DL winding is shown in [9] to perform better than the SL winding, but the DL slip-PMG is very difficult to manufacture. In this paper the SL winding is again considered due to its extremely simple construction. However, for the DL winding a slight modification is made. Instead of connecting the two adjacent non overlap coils in series, each coil is short-circuited individually.

978-1-4673-0803-8/12/$31.00 ©2012 IEEE

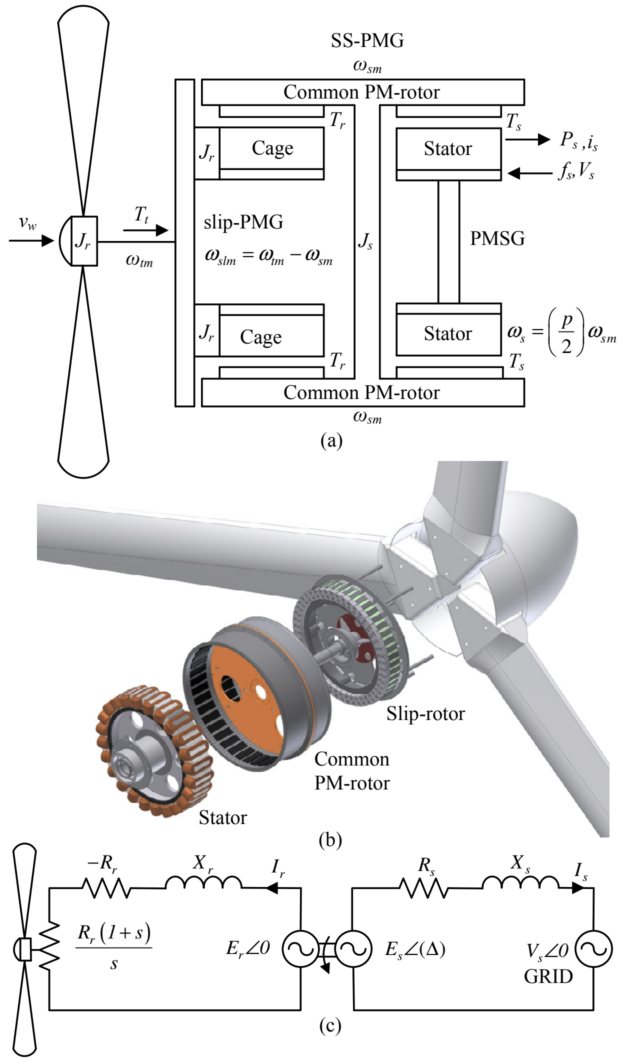

Fig. 2: (a) Cross section diagram, (b) example and (c) equivalent circuit of a new concept SS-PMG [9].

Against the contrary this alteration leads to a slight increase in the performance of the DL winding slip-PMG. More important, however, is the reduction in mechanical complexity.

To improve the torque performance of the slip-PMG a conventional 3-phase overlap cage winding as shown in Fig. 3(c) is investigated. The use of overlap cage windings, however, leads to a large torque ripple. An interesting observation was made with the evaluation of overlap cage winding slip-PMGs, that if the number of slots per pole is increased the torque ripple decreases accordingly. Also observed was that the current induced in each bar mimics the working of a brushless-DC machine as is shown and explained later in this paper. An example of such a machine structure is shown in Fig. 3(d).

The slot size of the brushless-DC slip-PMG as shown in the structure of Fig. 3(d) grows extremely small due to the large amount of slots. The smaller the slot size becomes, the more difficult it becomes to manufacture the machine, due to the problem of adequately fixing the bars to the end-rings. The bar-end-ring connection is extremely important and if the contact resistance becomes too large the torque performance of the machine is significantly reduced. For this reason the brushless-DC concept is also proposed as an axial flux machine as shown in Fig. 3(e). For an axial flux slip-PMG the cage can easily be manufactured as one solid piece. The solid cage can then be fixed to a solid steel disk, which acts as the slip-rotor yoke. In this case there is no contact resistance in the electrical circuit. Furthermore the manufacturing of the brushless-DC slip-PMG becomes much more realistic and in this case it is also possible to utilise a large part of the construction mass as part of the active mass in a typical wind generator topology. However, in this case single-rotor axial flux PM machines are known to have exceptionally large attraction forces between the PM-rotor and the slip-rotor.

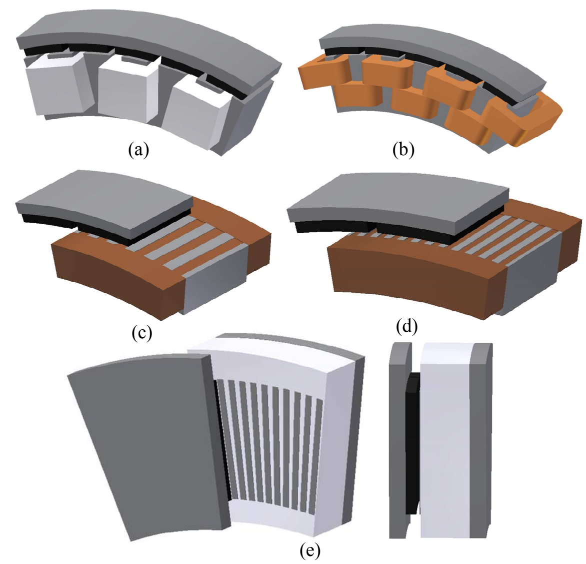

Fig. 3: (a) SL, (b) DL non overlap, (c) 3-phase overlap, (d) radial-flux brushless-DC and (e) axial-flux brushless-DC slip-PMG configurations.

III. Slip-PMG modelling

Two types of modelling are done for the slip-PMGs. The induced rotor bar currents of some of the slip-PMGs (DL and SL non overlap) are sinusoidal and these machines can be modelled in the *dq*-reference frame. However, for the brushless-DC slip-PMGs the current waveforms induced in the bars are trapezoidal or quasi-square-wave in nature. A flat topped DC magnitude is observed which corresponds to the magnet pitch (σ_m). Due to this flat current profile, the bar current is considered as a DC quantity during conduction which simplifies the modelling significantly.

A. DQ-Equivalent circuit modelling

From Fig. 4(a) the steady state *dq*-equations of the short circuited slip-PMG unit, with positive current taken as flowing out and I_{dr} and I_{qr} the *dq*-currents, are given by

$$0 = -R_r I_q - \omega_{sl}(L_d + L_e)I_d + \omega_{sl}\lambda_m \tag{1}$$

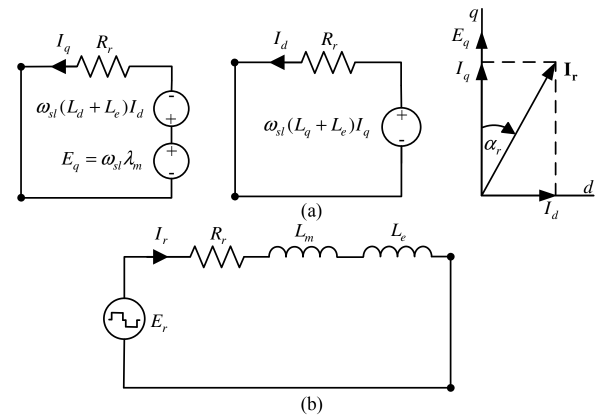

Fig. 4: (a) *DQ*-equivalent modelling and vector diagram and (b) brushless-DC modelling used to calculate the bar currents of the slip-PMG.

and

$$0 = -R_r I_d + \omega_{sl}(L_q + L_e)I_q \tag{2}$$

respectively where ω_{sl} is the electrical slip speed equal to $\omega_{sl} = \omega_t - \omega_s$, with ω_t the electrical turbine speed and $\omega_s = 2\pi f_s$, the electrical speed of the common PM-rotor. The *dq*-inductances in (1), (2) and Fig. 4(a), with λ_d, λ_q and λ_m indicating the *dq* and PM flux linkages respectively, are defined as

$$L_q = \frac{\lambda_q}{-I_q}; \qquad L_d = \frac{\lambda_d - \lambda_m}{-I_d}. \tag{3}$$

The per phase end-winding inductance is indicated by L_e in (1), (2) and Fig. 4(a) and can either be calculated by analytical methods or FE-analysis as discussed in [14]. The general relations of current and copper losses are given by (4) - (6) as

$$\begin{bmatrix} I_q \\ I_d \end{bmatrix} = \sqrt{2} I_{rms} \begin{bmatrix} \cos\alpha_r \\ \sin\alpha_r \end{bmatrix}, \tag{4}$$

$$I_q^2 + I_d^2 = 2I_{rms}^2, \tag{5}$$

and

$$I_{rms}^2 = \frac{P_{cu}}{3R_r}, \tag{6}$$

with P_{cu} the copper loss, R_r the per phase bar resistance and α_r the current angle. The developed torque of the slip-PMG is expressed as

$$T_r = \frac{3}{4}p[(L_q - L_d)I_d I_q + \lambda_m I_q]. \tag{7}$$

The efficiency is given by

$$\eta_r = \frac{P_r}{P_t} = \frac{T_r \omega_{sm}}{T_r \omega_{tm}} = 1 - s \tag{8}$$

where the subscript "*m*" in (8) donates mechanical speed and P_t and P_r respectively indicates the mechanical turbine input and the output power of the slip-PMG.

Another very important parameter in the design of the slip-PMG is the breakdown torque (T_b). However, calculating this parameter accurately is difficult. To get an indication of the value of this parameter ω_{sl} needs to be calculated where the derivative of (7) with respect to ω_{sl} is equal to zero. The first step is to rewrite (1) and (2) in order to have I_d and I_q in terms of ω_{sl}. This gives the following for I_d and I_q respectively as

$$I_d = \frac{\omega_{sl}^2 \lambda_m (L_q + L_e)}{R_r^2 + \omega_{sl}^2 (L_d + L_e)(L_q + L_e)} \tag{9}$$

and

$$I_q = \frac{\omega_{sl} \lambda_m R_r}{R_r^2 + \omega_{sl}^2 (L_d + L_e)(L_q + L_e)}. \tag{10}$$

By substituting (9) and (10) in (7) the following expression for T_r in terms of ω_{sl} is obtained as

$$\begin{aligned} T_r = \frac{3}{4}p\lambda_m^2 R_r &\left[\frac{\omega_{sl}^3 (L_q - L_d)(L_q + L_e)}{\left(R_r^2 + \omega_{sl}^2 (L_d + L_e)(L_q + L_e)\right)^2}\right] \\ &+ \frac{3}{4}p\lambda_m^2 R_r \left[\frac{\omega_{sl}}{\left(R_r^2 + \omega_{sl}^2 (L_d + L_e)(L_q + L_e)\right)}\right]. \end{aligned} \tag{11}$$

However, finding the derivative of (11) is a complex mathematical exercise. Observing (7) and knowing that $L_d \approx L_q$ for the machines considered, it can be concluded that the maximum torque is dominated by the term $\lambda_m I_q$. It would be much easier to find ω_{sl} where I_q is at a maximum. With I_q as given in (10)

$$0 = \frac{dI_q}{d\omega_{sl}} = R_r^2 - \omega_{sl}^2 (L_d + L_e)(L_q + L_e) \tag{12}$$

and finally

$$\omega_b \approx \frac{R_r}{\sqrt{(L_d + L_e)(L_q + L_e)}}. \tag{13}$$

The value for the breakdown slip speed, ω_b, calculated in (13) can now be used in (11) to calculate T_b. It is also shown in the results section of this paper that for these machines the torque curve has a very flat profile in the region of the breakdown torque. The calculated value of ω_b in (13) should, thus, be sufficient as slight variations in ω_{sl} will not influence the torque result significantly in the region of the breakdown torque.

B. Brushless-DC Modelling

For the brushless-DC machine, with the voltage waveform known to be square wave in nature, the flux waveform will be a triangular waveform. With each individual bar corresponding to one phase per pole section the parameters can be calculated per bar. Thus, with

$$E_r = N_r \frac{d\phi_r(t)}{dt} = \frac{\Delta\lambda}{\Delta t} \tag{14}$$

and with the peak flux linkage λ_r known and by observing the first quarter period of the flux waveform with $\Delta t = \frac{1}{4}T_{sl}$, E_r can be calculated from (15) as

$$E_r = \frac{p}{\pi}\lambda_r \omega_{slm} = K_r \omega_{slm}, \qquad \text{with} \qquad \omega_{slm} = \frac{4\pi}{p} f_{sl} \tag{15}$$

and with the armature reaction ignored and constant flux provided by the permanent magnets. The subscript *"m"* also donates mechanical speed in this case, f_{sl} is the electrical slip frequency and K_r is the machine constant.

From the equivalent circuit for the brushless-DC slip-PMG as shown in Fig. 4(b), the induced current of the machine can be calculated as in (16) with

$$I_r = \frac{E_r}{R_r} \tag{16}$$

with the bar resistance, R_r, calculated analytically from the given slot and end-ring dimensions. With I_r known the developed torque of the brushless-DC slip-PMG can be calculated for low slip values as

$$T_r = K_r I_r a \quad \text{with} \quad a = S \times \sigma_m. \tag{17}$$

The variable a in (17) indicates the effective number of bars active at any given time instance and is given as a function of the magnet pitch (σ_m) and the total number of slots (S) of the slip-rotor. With the brushless-DC slip-PMG known to have a very good torque performance the breakdown torque (T_b) is approximated with a per phase equivalent approach. For higher slip values, if the torque per bar is given as

$$T_r = \frac{I_r^2 R_r}{\omega_{slm}} \tag{18}$$

and with the voltage per bar as given in (15) the bar current can be written as

$$I_r = \frac{K_r \omega_{slm}}{\sqrt{R_r^2 + (\frac{p}{2} L_r \omega_{slm})^2}}. \tag{19}$$

By substituting (19) in (18), the torque is also given as

$$T_r = K_r^2 R_r \frac{\omega_{slm}}{R_r^2 + (\frac{p}{2} L_r \omega_{slm})^2}. \tag{20}$$

To obtain the maximum torque, ω_{slm} needs to be calculated where the derivative of (20) is equal to zero. Thus, with

$$0 = \frac{dT_r}{d\omega_{slm}} = -R_r^2 + (\frac{p}{2} L_r \omega_{slm})^2 \tag{21}$$

the mechanical slip speed where the maximum torque occurs, ω_{bm}, is given as

$$\omega_{bm} \approx \frac{2}{p} \frac{R_r}{L_r}. \tag{22}$$

By substituting (22) in (20) the breakdown torque (T_b) can finally be approximated as

$$T_b \approx \frac{K_r^2 a}{p L_r}. \tag{23}$$

The inductance specified by L_r includes the end-winding inductance as calculated analytically in [14].

C. FE Simulation Procedure

Due to the very large amount of optimisation results required for this study, it is beneficial that the solving time be reduced. Instead of using transient FE analysis that takes time, a number of non-linear static FE solutions are used in combination with the equations given above to simulate the state of the slip-PMG. The performance is calculated at a specified slip point in all cases. For both the machine types analysed, with *dq*-analysis, and brushless-DC modelling, a minimum of three static FE solutions are required to simulate the performance of the machine at a specific slip operating point. Fig. 5 shows the FE models and field plots of three of the different slip-PMG configurations, as discussed in Section II.

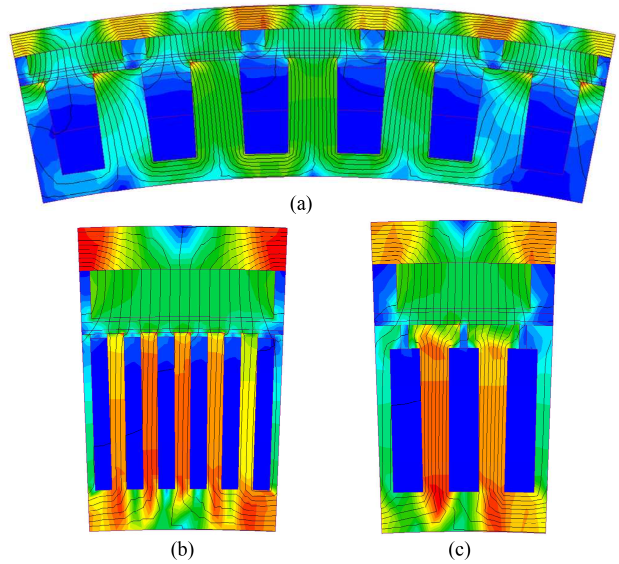

Fig. 5: FE-models and field plots (a) DL non overlap, (b) brushless-DC and (c) 3-phase overlap slip-PMG configurations.

1) FE combined with dq-modelling: For the slip-PMGs modelled by means of *dq*-equivalent modelling the same FE modelling procedure as thoroughly explained in [9] is used. A minimum of three static FE simulations are required to obtain the operating point and the performance of the machine at this point. The *abc*-flux linkages λ_{abc} are obtained at each static FE iteration. These flux linkages are transformed to the *dq* reference frame and are then used to solve (1)-(13) to obtain the operating point and performance of the machine. Due to L_d and L_q being dependent on the load point of the machine as shown in [9], better accuracy can be obtained by repeating the three static FE simulations at the value calculated for ω_b.

2) FE combined with brushless-DC modelling: To solve (15)-(23) for the brushless-DC machines the magnitude of the machine constant K_r is needed to calculated the flat topped DC quantity for E_r as in (15). By running one FE-simulation the peak flux linkage, λ_r, can be obtained and K_r can be calculated and (15)-(23) can be solved. However, especially for lower values of σ_m there is a dead band in the voltage waveform and a flat top in the flux linkage waveform, which influences the accuracy of the voltage calculation in (15). It would be better only to make use of the linear region of the flux linkage waveform, thus, by rather using two static FE simulations, two points, (t_1, λ_{r1}) and (t_2, λ_{r2}), can be obtained on the linear line which corresponds to the flat topped voltage waveform. E_r can now be calculated from (14), with $\Delta\lambda = \lambda_{r2} - \lambda_{r1}$ and $\Delta t = t_2 - t_1$, with the time steps calculated as $t = \theta_e / \omega_s l$

where θ_e is the electrical angle. With E_r known K_r can be calculated from (15) and finally (16) and (17) can be solved.

To calculate the breakdown torque of the brushless-DC machine, the total bar inductance, L_r, is needed. This value is calculated by exciting a amount of cage-rotor bars with rated current as calculated in (16) to take the mutual phase cross-coupling into account. The inductance can then be calculated as

$$L_r = \frac{\lambda_r}{I_r} + L_e \tag{24}$$

where λ_r is the flux linkage per bar. With L_r known (22) and (23) can be solved for ω_{bm} and T_b.

IV. Design Optimisation

The design optimisation is done by means of the *Visual Doc* optimisation suite. As in [9] the optimisation algorithm is coupled with the static FE-modelling methods as discussed above in Section III.

A. Optimisation Constraints and Methodology

All five of the machine structures discussed in Section II are optimised subject to certain design constraints for minimum active mass. These constraints are shown in Table I. The slip-PMG design is based upon a case study of a specific turbine configuration as discussed in [15]. The rated torque, T_r, corresponds to the torque value on the turbine curve at the rated power (P_r) and speed (n_s) as shown in Table I. For each of the optimised slip-PMGs the rated slip of $s_r = 0.03$ pu corresponds to an efficiency from (8) of 97 %. With the same PMSG unit currently being used as in [9] which has an efficiency of about 94 %, the total system efficiency is just over 91 %, which compares well with other wind turbine drive train topologies currently in use. In order to allow for stable operation of the directly grid-connected SS-PMG, previous practical iterations and dynamic studies seem to indicate a no-load cogging torque ($\Delta\tau_{NL}$) of not more than 2.5 % and a load torque ripple ($\Delta\tau_L$) of not more than 4 %.

Although a minimum active mass for the slip-PMG is important to limit the mass footprint of adding a second PM generator to the design, manufacturing cost is also important. With the price of rare earth PMs currently very volatile such a design optimisation where cost is taken into account makes sense. However, due to the different construction methods and manual labour requirements for the different slip-PMGs adding a cost to these different machines is difficult. To allow for some sort of cost optimisation, the slip-PMGs are also optimised by putting different constraints on the amount of PM material that may be utilised. Also with Aluminium much cheaper than Copper, both Aluminium and Copper are considered for the conductor material.

B. Optimisation Results

The optimisation results for the five different slip-PMG topologies as shown in Fig. 3 are given in Table II for the SL and DL slip-PMGs and Table III for the 3-phase overlap and radial and axial flux brushless-DC slip-PMGs. The two dimensions given are the axial stack length (l) and the inside diameter (D_i) of the machine. The mass quantities shown are the PM mass (M_{PM}), conductor mass (M_C), steel mass (M_{Fe}) and the total active mass (M_{Tot}). The different slip-PMG configurations are also evaluated regarding the complexity and ease of construction.

As far as possible the aim was to keep the PM content the same for all the machine configurations in order to have a more

TABLE I: Design constraints of the slip-PMG.

Parameter	Value
Rated torque (T_r), Nm	1000
Rated slip (s_r), pu	0.03
Breakdown torque (T_b), pu	≥ 2.0
No load torque ripple ($\Delta\tau_{NL}$), %	≤ 2.5
Full load torque ripple ($\Delta\tau_L$), %	≤ 4.0
Synchronous speed (n_s), $\mathrm{r.min}^{-1}$	150
Electrical output power (P_s), kW	15
Maximum outside diameter (D_o), mm	655

TABLE II: Optimisation results of the SL and DL non overlap slip-PMGs.

	Non overlap-SL		**Non overlap-DL**	
	Al	Cu	Al	Cu
T_b, pu	2.00	2.02	2.01	2.11
$\Delta\tau_{NL}$, %	2.54	1.43	1.65	1.94
$\Delta\tau_L$, %	3.12	3.91	1.18	1.82
l, mm	131.8	124.7	107.1	90.50
D_i, mm	579.0	593.0	562.0	578.0
M_{PM}, kg	5.57	5.08	5.62	4.48
M_{cond}, kg	12.2	21.5	12.5	23.2
M_{Fe}, kg	43.0	34.5	38.3	33.1
M_{Tot}, kg	60.7	61.1	56.3	60.8

Notes:

Non overlap-SL
Extremely simple construction. Easy use of Aluminium. No contact resistance. High mass and PM content. Long stack length might be a problem.

Non overlap-DL
Easy construction. Easy use of Aluminium. No contact resistance. High mass and PM content, but lower than SL.

TABLE III: Optimisation results of the 3-phase overlap and brushless-DC slip-PMGs.

	Overlap 3-phase		**Brushless-DC radial Flux**		**Brushless-DC axial Flux**	
	Al	Cu	Al	Cu	Al	Cu
T_b, pu	2.02	2.02	2.03	2.40	2.10	2.39
$\Delta\tau_{NL}$, %	5.56	3.76	1.64	1.97	1.33	0.93
$\Delta\tau_L$, %	10.78	9.94	0.44	0.71	2.28	2.61
l, mm	82.0	66.5	62.5	55.0	55.5	44.6
D_i, mm	565.0	577.0	570.0	580.6	490.0	533.2
M_{PM}, kg	3.53	3.43	3.53	3.51	3.62	3.49
M_{cond}, kg	8.99	17.05	7.22	12.38	10.16	16.34
M_{Fe}, kg	28.18	20.14	22.25	15.98	14.97	6.97
M_{Tot}, kg	40.70	40.62	33.0	31.87	28.76	26.80

Notes:

Overlap 3-phase
Moderate to difficult construction. Possible Aluminium casting. Contact resistance a problem. Medium to low mass and low PM content. High torque ripple.

Brushless-DC-radial
Very difficult construction. Aluminium use might be difficult. Contact resistance a problem. Low mass and PM content. Low torque ripple.

Brushless-DC-axial
Moderate to easy construction. Easy use of Aluminium. No contact resistance. Very low mass and PM content. Large attraction forces.

valid comparison of the active mass. This is true for the results shown in Table III, but for the non overlap winding machines a much higher PM content is needed. The relationship between M_{Tot} and M_{PM} are shown in Fig. 6. The mass results shown are for the SL and DL non overlap slip-PMGs using Copper as a conductor, and for the brushless-DC radial and axial flux configurations with both Copper and Aluminium used as a conductor. The values for M_{PM} shown in Table II for the SL and DL slip-PMGs are the lowest PM margin which can be specified for these machines as also shown in Fig. 6, while still complying with the constraints given in Table I. For the brushless-DC machines an optimum of more or less M_{PM} = 3.5 kg is found. Specifying a higher PM mass does not lead to a significant decrease in active mass.

From Tables II and III it is clear that the brushless-DC slip-PMG configurations yields a much lower active mass and lower PM content due to the much better torque performance of these winding types. This is especially true for the axial flux machine where parts of the construction mass and active mass can be combined as mentioned.

Furthermore surprising results are obtained when optimisations are done for different conductor materials specified. The use of Copper instead of Aluminium as conductor material does not necessarily lead to a significantly better performance regarding active mass. Furthermore the Aluminium machines have a much lower value for M_C and it should also be noted that Aluminium is about four to five times cheaper than Copper. It is true that the Aluminium machines have a higher value for M_{Fe}, but steel is even cheaper than Aluminium. Thus, for the same PM mass the Aluminium machines are much cheaper per kilogram than the Copper machines. An advantage of the Copper machines, however, is that a slightly lower PM mass can be specified. This is also shown in Fig. 6 where the minimum PM mass shown for all the graphs is also the minimum PM mass where the machines still comply with the specifications of Table I. The Copper machines yield a lower minimum PM mass due to the fact that the Aluminium machines have a larger steel volume which increases the per phase inductance which in turn influences the value for the maximum torque as shown in (11) and (23). The relationship between the inside diameter, D_i, and the average and breakdown torque is shown in Fig. 7.

Although the optimisation results for minimum active mass in Tables II and III indicate substantial per unit differences between the different configurations it should be noted that the mass decrease for the whole SS-PMG wind turbine system will be significantly different. Thus, for a case study and initial evaluation the PMSG and wind turbine system as discussed in [9], [10], [15] is used. For this SS-PMG wind turbine system the total tower top mass if only the PMSG is included, is measured at about 500 kg. For all the slip-PMG configurations in Tables II and III the same construction mass of more or less 40 kg needs to be added. To put the mass results of Tables II and III in perspective the total SS-PMG tower top mass, M_{Top}, is estimated as $M_{Top} = 500 + 40 + M_{Tot}$ kg. Thus, the highest mass slip-PMG yields a total mass increase of 1.2 pu while the lowest mass slip-PMG yields a total mass increase of 1.12 pu.

From an overall mass perspective it would not make much difference which of the slip-PMG configurations are selected. The decision will mostly be governed by cost. Cost, however, is difficult to fix due to the volatility of raw material prices especially regarding the rare-earth PM materials. Furthermore, the construction methods can also largely influence the cost, with the non overlap machines much cheaper to manufacture than the rest. Also the manufacturing methods for Aluminium and Copper are not always the same with the manufacturing methods used for Copper more expensive in some cases.

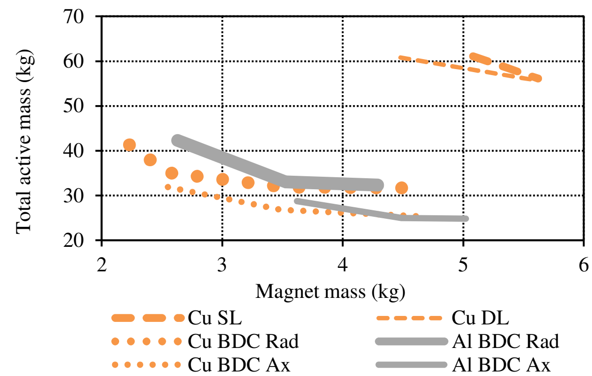

Fig. 6: Active mass versus PM mass for the non overlap SL and DL and the brushless-DC (BDC) radial (rad) flux and axial (ax) flux slip-PMGs.

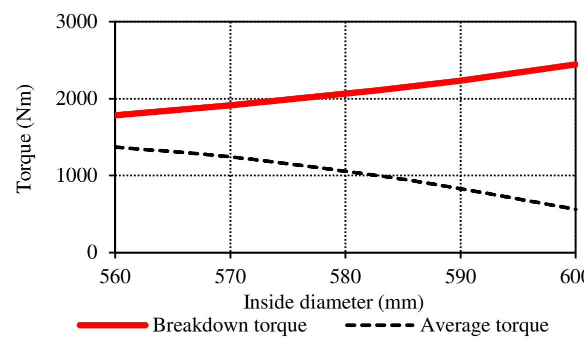

Fig. 7: Average and breakdown torque versus inside diameter for the DL slip-PMG.

V. Simulation Results

For the practical evaluation three prototype slip-PMG configurations are considered. The simulation results for only these three machines are shown as these are the only slip-PMG configurations which were manufactured and practically evaluated. These three configurations are the non overlap DL and SL slip-PMGs shown in Fig. 3(a) and (b) repectively and the brushless-DC slip-PMG as shown in Fig. 3(d). The prototype machines are shown in Fig. 8 for the SL, DL and brushless-DC slip-PMGs respectively. It should be noted that these machines are not optimum designed slip-PMG configurations as in Tables II and III. The machines in this section are merely used to validate the operating principles of the various technologies and also to verify the FE results. The DL slip-PMG makes uses of a wounded slip-rotor due to the difficulty of connecting the two adjacent solid bar-coils in series. To test the performance of the new novel DL concept as discussed in this paper, the series connections in Fig. 8(b) are removed and each coil is short-circuited individually. The SL machine is a very simple unoptimised structure which fits within the dimensions of the DL machine in Fig. 8(b) and makes use of solid bar-coils as shown in Fig. 8(a).

Due to the difficulty of fixing the very thin bars of the brushless-DC slip-PMG to the end-rings and the problem of contact resistance, a different approach is followed for the construction of this machine. In this case each bar is an individually short-circuited coil with the current return path underneath the stack as shown in Fig. 8(c). These solid bar coils are cut from very thin sheets of Aluminium. The coils are shifted into position through a central opening in the lamination stack which is filled up after all the other coils are in position. Although this is not an optimum solution due to the very long current path and, thus, high resistance, this prototype is sufficient to validate the concept of a brushless-DC slip-PMG.

Fig. 9 shows the torque versus slip profiles of the three different non overlap slip-PMG prototypes and the brushless-DC slip-PMG. The DL winding machines have a much higher breakdown torque value than the SL winding slip-PMG in this case. Also the slightly better performance of the new concept DL winding machine (DL2) is clearly seen as opposed to the conventional DL winding (DL1). The breakdown torque of the prototype brushless-DC machine on the other hand is more than double that of the DL2 winding slip-PMG. What is interesting is that in this case all three slip-PMGs have more or less a similar mass and PM content. It is, thus, evident that for the same active and PM mass the brushless-DC-machine has a much better torque performance.

In Fig. 10 the measured and FE-simulated cogging torque of the SL slip-PMG is shown and also the FE-simulated load torque ripple of the DL non overlap slip-PMG. Fig. 11 shows the FE simulated and measured cogging torque and also the FE simulated load torque ripple of the brushless-DC slip-PMG. This clearly indicates the very low torque ripple of the brushless-DC winding. Fig. 12 shows the sinusoidal induced current per bar coil of the SL slip-PMG and the quasi-square current waveform of the brushless-DC slip-PMG simulated by means of FE. The measured grid voltage and current of the prototype SS-PMG system connected directly to the grid at almost full load is shown in Fig. 13.

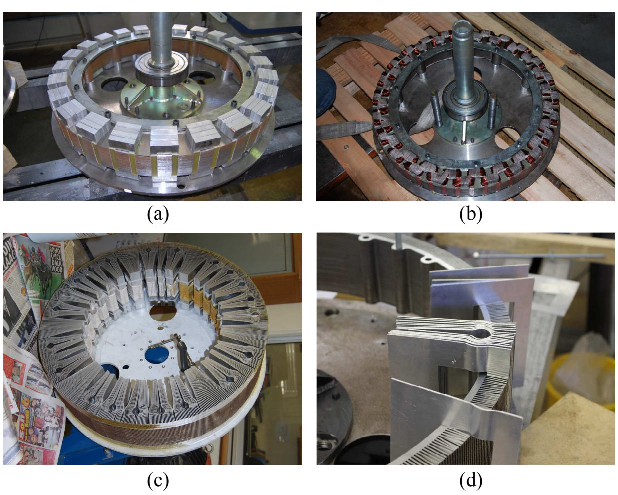

Fig. 8: (a) SL non overlap, (b) DL non overlap, (c) brushless-DC slip-PMG prototype slip-rotors and (d) thin solid bar-coils being shifted into position for the brushless-DC slip-PMG.

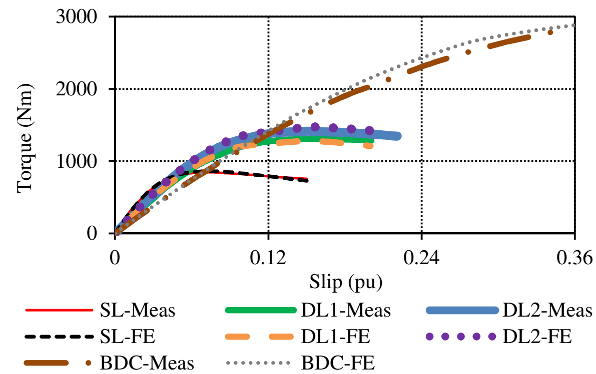

Fig. 9: Measured and FE calculated torque versus slip of the prototype non overlap single layer, the conventional series connection double layer winding (DL1), the new concept individually short-circuited coil double layer winding (DL2) and brushless-DC (BDC) slip-PMGs.

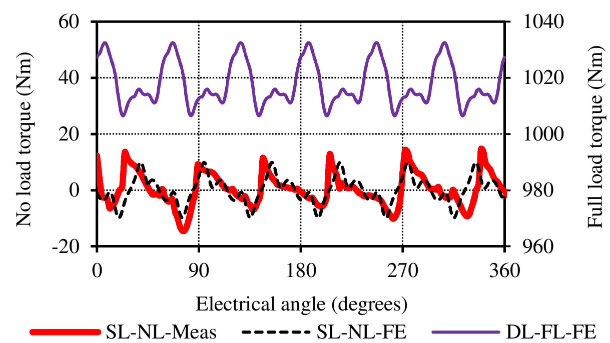

Fig. 10: Measured and FE calculated no-load (NL) cogging torque for the SL and FE calculated full-load (FL) torque ripple for the DL versus electrical angle of the prototype non overlap slip-PMGs.

VI. Conclusion

In this paper it is shown that the active mass of the slip-PMG unit in a SS-PMG can be minimised significantly. Several new slip-PMG concepts are evaluated. Especially for the novel brushless-DC winding slip-PMG a significant reduction in active and PM mass as opposed to the non overlap winding configurations is possible. Furthermore it is shown that aluminium can be used instead of copper without significantly increasing the mass of the slip-PMG for the same performance. The use of aluminium can lead to a significant reduction in the cost of the machine. However, construction, especially regarding

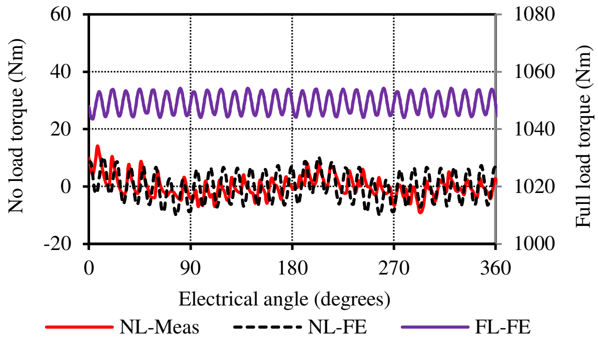

Fig. 11: Measured and FE calculated no-load (NL) and FE calculated full-load (FL) torque ripple for the brushless-DC prototype slip-PMG versus electrical angle.

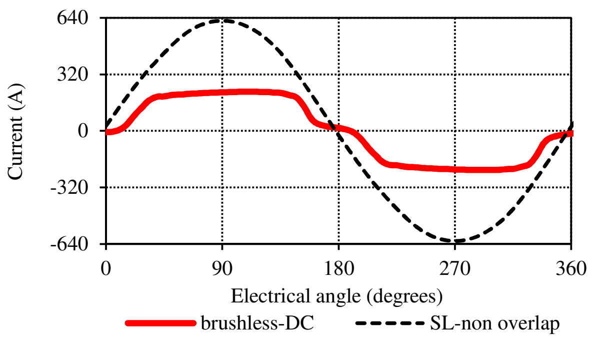

Fig. 12: FE calculated rated bar current of the SL-non overlap and brushless-DC prototype slip-PMGs versus electrical angle.

the fixing of the bars to the end-rings, poses a significant challenge for the brushless-DC slip-PMG. Other brushless-DC concepts like for instance the axial-flux configuration are, thus, evaluated to reduce the complexity of fixing the bars to the end-rings. The axial flux machine yields an especially low active mass due to the fact that some of the construction and active parts of the machine can be integrated. However, the large attraction forces associated with this machine is a problem. The conventional 3-phase overlap winding also shows promising results for the active mass reduction and torque performance, but torque ripple is still a question in this regard. Construction wise the non overlap winding machine types are by far the easiest to manufacture. Although the active masses of the non overlap winding PM machines are much higher than those of the brushless-DC machines, the total tower top mass increase ranges from 1.12 pu for the lightest slip-PMG configuration to 1.2 pu for the heaviest slip-PMG configuration. From an overall mass perspective active mass is, thus, not that critical in the choice of slip-PMG configuration. However, the brushless-DC type machine can be optimised to use a much lower amount of PM material. With rare earth PMs very expensive and due to the volatility of the PM price, the eventual choice of slip-PMG will be determined by the PM cost of the day versus the cost and methods of manufacturing available.

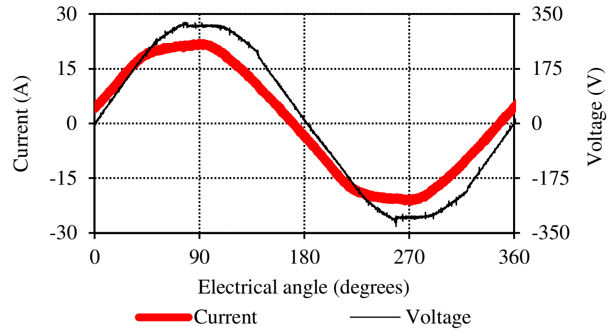

Fig. 13: Measured current and grid voltage at almost full load of the prototype SS-PMG versus electrical angle.

REFERENCES

[1] F. Punga and L. Schon, "Der neue kollektorlose Einphasenmotor der Firma Krupp," *Elektrotechnische Zeitschrift*, vol. 47, no. 29, pp. 877–881, 1926.

[2] J. F. H. Douglas, "Characteristics of induction motors with permanent-magnet excitation," *AIEE Trans. Part III: Power Apparatus and Systems*, vol. 78, no. 3, pp. 221–225, 1959.

[3] J. K. Sedivy, "Induction motor with free-rotating DC excitation," *IEEE Trans. Power Apparatus and Systems*, vol. 86, no. 4, pp. 463–469, 1967.

[4] W. F. Low and N. Schofield, "Design of a Permanent Magnet Excited Induction Generator," in *Proc. of Int. Conf. on Electrical Machines (ICEM'92)*, Manchester, United Kingdom, 1992.

[5] B. Hagenkort, T. Hartkopf, A. Binder, and S. Jöckel, "Modelling a direct drive permanent magnet induction machine," in *Proc. of Int. Conf. on Electrical Machines (ICEM'00)*, Espoo, Finland, 2000.

[6] E. Troster, M. Sperling, and T. Hartkopf, "Finite element analysis of a permanent magnet induction machine," in *International Symposium on Power Electronics, Electrical Drives, Automation and Motion, (SPEEDAM 2006)*, Taormina(Sicily), Italy, 2006.

[7] Y. Shibata, N. Tsuchida, and K. Imai, "High torque induction motor with rotating magnets in the rotor," *Electrical Engineering in Japan*, vol. 117, no. 3, pp. 102–109, 1996.

[8] T. Fukami, K. Nakagawa, R. Hanaoka, S. Takata, and T. Miyamoto, "Nonlinear modeling of a permanent-magnet induction machine," *Electrical Engineering in Japan*, vol. 144, no. 1, pp. 58–67, 2003.

[9] J. H. J. Potgieter and M. J. Kamper, "Design of new concept gearless direct-grid connected slip-synchronous permanent magnet wind generator," *IEEE Trans. on Industrial Applications*, vol. 48, no. 3, pp. 913–922, 2012.

[10] ——, "Torque and voltage quality in design optimisation of low cost non-overlap single layer winding permanent magnet wind generator," *IEEE Trans. on Industrial Electronics*, vol. 59, no. 5, pp. 2147–2156, 2012.

[11] A. Westlake, J. Bumby, and E. Spooner, "Damping the power-angle oscillations of a permanent-magnet synchronous generator with particular reference to wind turbine applications," *IEE Proc. Electric Power Applications*, vol. 143, no. 3, p. 269, 1996.

[12] S. Grabic, N. Celanovic, and V. Katic, "Permanent Magnet Synchronous Generator Cascade for Wind Turbine Application," *IEEE Trans. on Power Electronics*, vol. 23, no. 3, pp. 1136–1142, 2008.

[13] H. Muller, M. Poller, A. Basteck, M. Tilshcher, and J. Pfister, "Grid compatibility of variable speed wind turbines with directly coupled synchronous generator and hydro-dynamically controlled gearbox," in *Sixth International Workshop on Largescale integration of wind power and transmission networks for offshore wind farms*, Delft, Netherlands, 2006.

[14] J. H. J. Potgieter and M. J. Kamper, "Evaluation of calculation methods and the effects of end-winding inductances on the performance of non-overlap winding PM machines," in *Proc. Int. Conf. on Electrical Machines*, Marseille, France, 2012.

[15] J. H. J. Potgieter, "Design and analysis of a gearless direct grid permanent magnet induction generator," Master's thesis, University of Stellenbosch, Stellenbosch, South Africa, 2011.